# STATUS AND PROSPECTS OF THE CERN-LHC EXPERIMENT ALICE*

H.R. Schmidt

for the ALICE Collaboration

Gesellschaft für Schwerionenforschung mbH
64291 Darmstadt, Germany

*(Received April 15, 2002)*

An overview of the prevailing experimental conditions at the CERN-LHC for heavy-ion collisions is given. Observables, in particular those unique to the LHC energy regime, are discussed. The experimental challenges and physics potential of detector subsystems — TPC and TRD — are reviewed in some detail.

PACS numbers: 25.75.–q

## 1. Introduction

The quest for ever increasing heavy-ion beam energies has a simple, but fundamental cause in the very subject of ultra-relativistic heavy-ion collisions: the prerequisite to access the physics of QCD thermodynamics is the preparation of a system of high energy density and of long lifetime or, equivalently, large system size. Yet, ultra-relativistic heavy-ion collisions, often dubbed as the physics of the early universe, will never be able to reach the conditions of the "big bang" QCD phase: a macroscopic system size of the order of $10^{48}$ fm$^3$ and life time of $10^{18}$ fm$/c$ — truly justifying a thermal description. However, with the advent of heavy-ion colliders (RHIC, LHC), augmenting the center-of-mass energy in heavy-ion collisions by orders of magnitude (see Table I) as compared to fixed target collisions, macroscopic conditions will be reachable at least on a relative scale: the scale variable $\Lambda_{\rm QCD} = 200$ MeV will be surpassed by almost an order of magnitude. The same will be true for both the system size and the lifetime which will be large compared to the relevant scale of $\approx 1$ fm.

* Presented at the Cracow Epiphany Conference on Quarks and Gluons in Extreme Conditions, Cracow, Poland, January 3–6, 2002.

## 2. Initial conditions

"Conventional" scaling as known from elementary proton–proton collisions, yields only a very slow logarithmic increase in particle multiplicity and average transverse momentum with the center-of-mass energy ($\sqrt{s}$) [1,2]. There are, however, several mechanisms valid in ultra-relativistic heavy-ion collisions which change the $\log(\sqrt{s})$ dependence drastically:

(a) The scaling of the multiplicity $dN/dy$ with the mass of the projectile changes from $N_{\rm part}$, *i.e.*, the number of projectile nucleons participating in the reaction, to $N_{\rm coll}$, *i.e.*, the number of collisions, when going from low (SPS) to high (LHC) center-of-mass energies. While $N_{\rm part}$ is essentially given by the geometrical overlap, *i.e.*, is proportional to $A$, $N_{\rm coll}$ scales like $A^{4/3}$. This change, essentially due to the change from soft to hard collisions, yields an increase in $dN/dy$ up to a factor of 6 at LHC compared to SPS (dependent on relative contributions of soft and hard processes in the collision) [3, 4].

(b) At high energies, the projectile partons probe the low-$x$ region. The gluon structure function rises strongly at small-$x$ [5] leading to a high-density initial parton cascade with rapid thermalization [6]. The number of gluons per nucleon increases by a factor 8 from SPS to LHC energies [7]. The increase might, however, be reduced by a factor of two by nuclear gluon shadowing [6, 8, 9].

(c) The increased energy loss of hard partons in gluon matter ("jet quenching") [10], essentially fragmenting a jet into many soft particles, will further substantially increase the final state multiplicity. On the other hand, $dN/dy$ might be reduced by effects like parton saturation, both in the initial and the final state [11].

The investigations of the role of hard processes is subject of intense experimental investigations at RHIC [8, 12]. Theoretically, hard processes are accessed via pQCD calculations. At present, the extrapolation from the RHIC experimental results and the theoretical uncertainties of the pQCD calculations do still have large error bars [3]. Thus, the prediction of the LHC $dN_{\rm charged}/dy$ is uncertain and ranges from 3000 to 8000 charged particles per unit rapidity in a central collision.

## 3. Fireball evolution

In the following the evolution of a fireball is described assuming initial conditions as outlined above, *i.e.*, an initial temperature of 1 GeV, a thermalization time of the parton cascade $\ll 1$ fm/$c$ and a final state multiplicity

$dN_{\rm charged}/dy$ of 8000 particles. Details of the calculations can be found elsewhere [13]. In this picture a partonic fireball with an initial energy density of $\varepsilon_i \approx$ 1000 GeV/fm$^3$ expands dominantly longitudinally (Bjorken-picture). After the "canonical" formation time $\tau_0 = 1$ fm/$c$, the energy density is still 40 GeV/fm$^3$. The system is assumed to undergo a first order phase transition at $T_{\rm c} = 170$ MeV. Hadronization is completed after 35 fm/$c$, *i.e.*, the system has spent a significant time in the QGP and mixed phase. Thermal freeze-out takes place at $T_{\rm f} \approx$ 120 MeV; until then the system has lived about 70 fm/$c$. At freeze-out ($n_{\rm f} = 0.12$ fm$^{-3}$) the final volume occupied by the particles is $10^5$ fm$^3$, significantly larger than typical hadron sizes and mean free paths. Altogether, it seems to be justified to say that in LHC Pb + Pb collisions conditions are created which justify a description employing QCD thermodynamics, *i.e.* quarks and gluons being in thermal equilibrium.

The system parameters of Pb + Pb collisions at LHC energies are summarized in Table I and compared to those from reactions at SPS and RHIC energies.

TABLE I

Comparison of some system parameters prevailing at SPS, RHIC and LHC energies for heavy-ion collisions.

| | SPS | RHIC | LHC |
|---|---|---|---|
| $E_{\rm cm}$ [GeV] | 17 | 200 | 5500 |
| $dN_{\rm ch}/dy$ | 500 | 700 | 3000–8000 |
| $\varepsilon_{\rm Bj}$ [Gev/fm$^3$]$_{\tau_0=1\,{\rm fm}/c}$ | $\approx 2.5$ | $\approx 3.5$ | 15–40 |
| $V_{\rm freeze}$ [fm$^3$] | $\approx 10^3$ | $\approx 9\times 10^3$ | $\approx 3.7\times 10^4$–$1.0\times 10^5$ |
| $\tau_{\rm QGP}$ [fm/$c$] | $<1$ | $\approx 1$ | $\approx 4.5$–12 |

As can be seen from the Table the relevant system parameters, *i.e.*, QGP lifetime $\tau_{\rm QGP}$, energy density $\varepsilon_{\rm Bj}$ and freeze-out volume $V_{\rm freeze}$ increase substantially from SPS to LHC.

## 4. Observables and probes

The observables in heavy-ion collisions and probes of QGP formation are numerous and reviewed in many articles, *e.g.* [14]. Here we concentrate on those which are either unique to the LHC energies and/or to the ALICE experimental apparatus.

### 4.1. $dN/dy$ (multiplicities)

As outlined above, final state multiplicities are influenced to a large extent by initial state processes described theoretically by perturbative QCD. The uncertainties in the calculations are substantial. In turn, the measurement of $dN/dy$ [8, 12] will shed light onto initial state processes. As an example, figure 1 shows the distribution $dN/d\eta$ as calculated in HIJING, both with and without energy loss of partonic jets via gluon bremsstrahlung. As can be seen, the dependence on the process is sizable. Similarly, parton saturation is expected to influence considerably the final state multiplicities. At LHC, and to a smaller extent also at RHIC, the density of low-$x$ gluons, both in the incoming nuclei as well as after scattering, becomes so large that the available transverse space is completely occupied with gluons having a "radius" of $\sim 1/p_{\mathrm{T}}$ and the density of gluon "saturates" thus limiting the multiplicity. Nuclear shadowing of gluons might play a similar role. These processes are expected to set in around 2 GeV/$c$ at the LHC [15], *i.e.*, where pQCD is applicable and theoretical concepts can be tested.

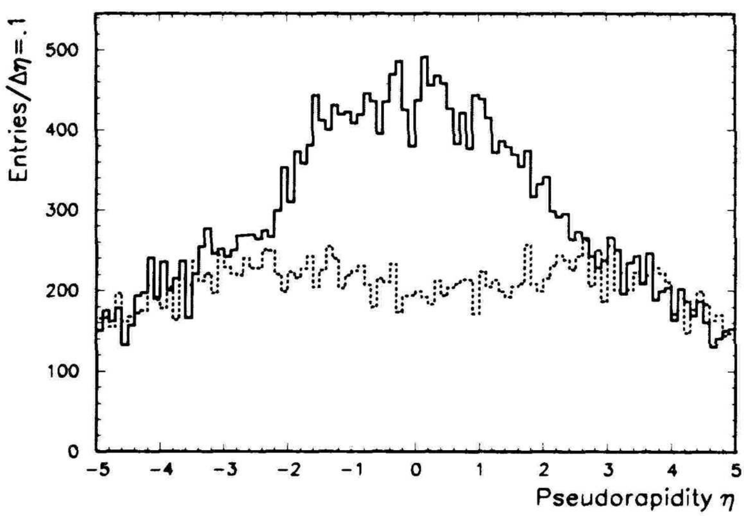


Fig. 1. Rapidity distribution of charged particles for two central Pb + Pb collisions as generated by the HIJING generator, with (full line) and without (dashed line) the effect of "jet quenching" in the medium.

### 4.2. Event-by-Event analysis

A feature which is truly unique to LHC Pb + Pb collisions is that Event-by-Event (EbE) studies, pioneered by the NA49 collaboration at the SPS for $\pi$'s and $K$'s [16], can be extended to particle species previously not accessible to EbE-physics. Table II gives a list of particles with abundances high enough to allow the investigation of non-statistical fluctuations on an EbE basis. These fluctuations are generally associated with critical phenomena at phase boundaries. Even in the absence of critical phenomena the increased precision ($\approx 1/\sqrt{N}$) will allow to correlate (inclusive) variables, *e.g.* temperatures measured via $p_{\mathrm{T}}$-spectra, radii measured via HBT or the event-plane measured via elliptic flow on an Event-by-Event basis.

TABLE II

Rapidity densities of various particles for Pb + Pb central collisions as predicted by thermal model calculations [17]. Chemical freeze-out takes place at $T = 170$ MeV in a volume of 14400 fm$^3$.

| Species | $dN/dy$ (ALICE) |
|---|---|
| $\pi^- \approx \pi^+ \approx \pi^0$ | 2500 |
| $K^+ \approx K^- \approx K_0^s$ | 385 |
| $\gamma$ | 500 |
| $\bar{p} \approx p$ | 250 |
| $\bar{\Lambda} \approx \Lambda$ | 126 |

### *4.3. Hard processes*

Hard processes, *i.e.*, scatterings with large momentum transfer, become dominant at LHC. These processes, in particular high $p_{\mathrm{T}}$-jets and heavy vector meson production, can be used to probe the early stages of the reaction. Figure 2 shows the energy density dependence of the survival probabilities of quarkonia states ($J/\Psi$ and $\Upsilon$-family) expected in a deconfined medium and by absorption in a hadronic environment. The "classical" deconfinement signal, *i.e.*, $J/\Psi$ suppression, has recently been reinvestigated and it has been found: (a) that the suppression signal is partly obscured by a sequential suppression pattern setting in already below the critical temperature due to in-medium modification of the open charm threshold as well as the $J/\Psi$ mass itself [14, 18]; and (b) that statistical hadronization of the — at RHIC and LHC — abundantly produced $c\bar{c}$-pairs might compensate the suppression signal at RHIC and even lead to $J/\Psi$ enhancement at LHC [19].

A "clean" suppression signal is expected from the tightly bound $\Upsilon$. This particle, however, is produced with sufficient statistics only at LHC (the cross sections at RHIC are one order of magnitude lower). Moreover, energy densities above the melting point of the $\Upsilon$ ($\varepsilon > 20$ GeV/fm$^3$) can be reached only at the LHC. A comprehensive measure of the both the $J/\Psi$ and the $\Upsilon$-family is therefore of outmost importance in ALICE.

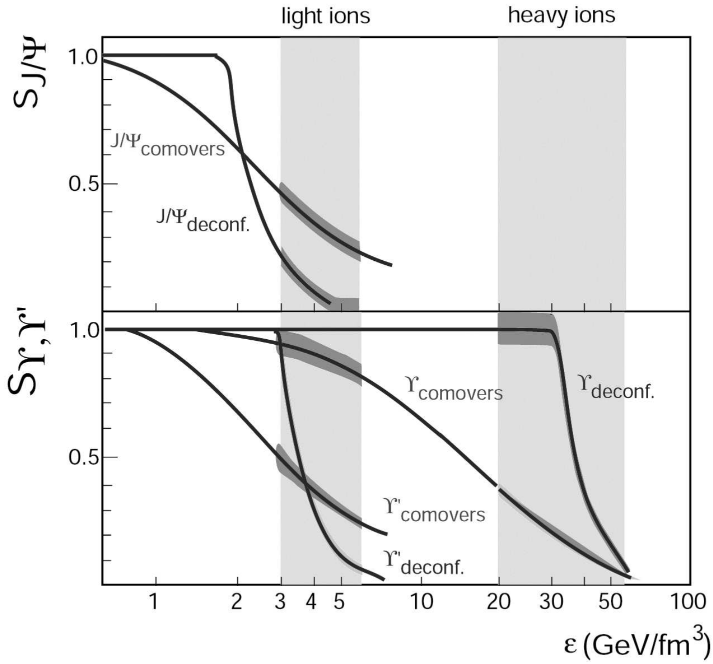


Fig. 2. Energy density dependency of charmonium and bottonium survival probabilities as expected from melting in a deconfined medium and from the comover model. The precision of the measurement in ALICE after one month of running is shown as $1\sigma$ error bands.

Moreover, because of the intimate connection between charmonium and bottonium states and open charm/bottom [20] the measurement of $D$ and $B$ mesons is essential in ALICE.

"Jet-quenching", *i.e.*, the energy loss of hard partons via partonic matter, is a new probe not available at the SPS. First hints of this mechanism might have been visible at RHIC in form of altered shapes of hadron $p_{\mathrm{T}}$-spectra [21]. At LHC, with the dominance of hard collisions, the measurement of jet cross section and fragmentation functions will be a major probe of the earlier stages of the collision.

## *4.4. Photons*

Real or virtual photons, emitted from the QGP, carry the promise of yielding undisturbed information from this phase. However, the difficulties to measure photons, in particular to disentangle the rare single, thermal photons emitted from a potential QGP from those of other sources are enormous. This is schematically depicted in figure 3 [22], which shows the different sources of photons. While at low $p_{\mathrm{T}}$ the background from $\pi^0$ decay is overwhelming (it can, however, be measured and subtracted with a precision of about 5%), thermal plasma photons compete with photons from the hadron phase at medium and with QCD photons at high $p_{\mathrm{T}}$. It will evidently be rather challenging to disentangle the contribution of the different sources.

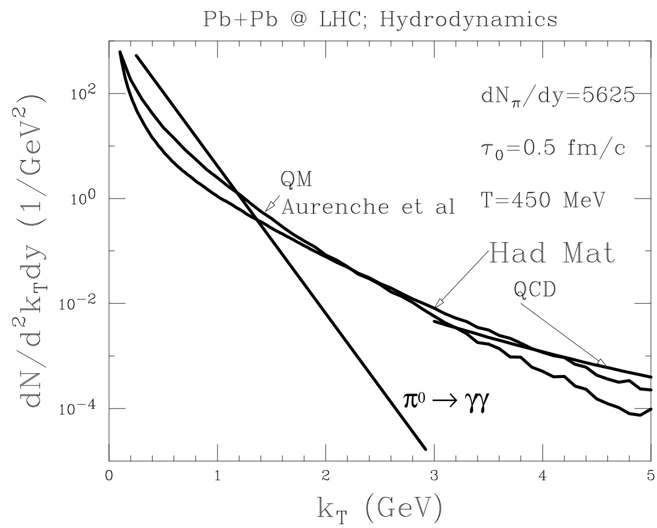


Fig. 3. Schematic distribution of single photons from different sources.

## 5. The LHC

The LHC will potentially start to collide protons at $\sqrt{s} = 14$ TeV in early 2006 and will provide the first heavy-ion collisions (Pb–Pb) towards the end of its first year of operation at a total c.m.s. energy of 1148 TeV ($\sqrt{s} = 5.5$ TeV per nucleon for Pb–Pb). The sharing between proton and ion runs is expected to be similar to the one used in the past at the SPS, *i.e.*, a long proton run ($10^7$ s effective time) followed by a few weeks ($10^6$ s) of heavy-ion or proton–nucleus collisions. The ion luminosity is limited for heavy systems by the short beam life-time and by the energy deposition in the super-conducting machine magnets (quench protection). It reaches values between $3 \times 10^{31}$ cm$^{-2}$s$^{-1}$ for light ions ($O^{16}$) and $10^{27}$ cm$^{-2}$s$^{-1}$ for Pb ions. Proton– or deuteron–nucleus collisions are feasible and foreseen, however, only at equal magnetic rigidity per beam as the bending field is identical in both rings ('two-in-one' magnet design of the LHC). Further information on heavy-ion operation of the LHC can be found in Ref. [23].

## 6. The ALICE experiment

ALICE is a general-purpose heavy-ion detector designed to study the physics of strongly interacting matter and the quark–gluon plasma in nucleus–nucleus collisions at the LHC. The Collaboration currently includes more than 900 physicists and senior engineers — both from nuclear and high-energy physics — from about 77 institutions in 28 countries.

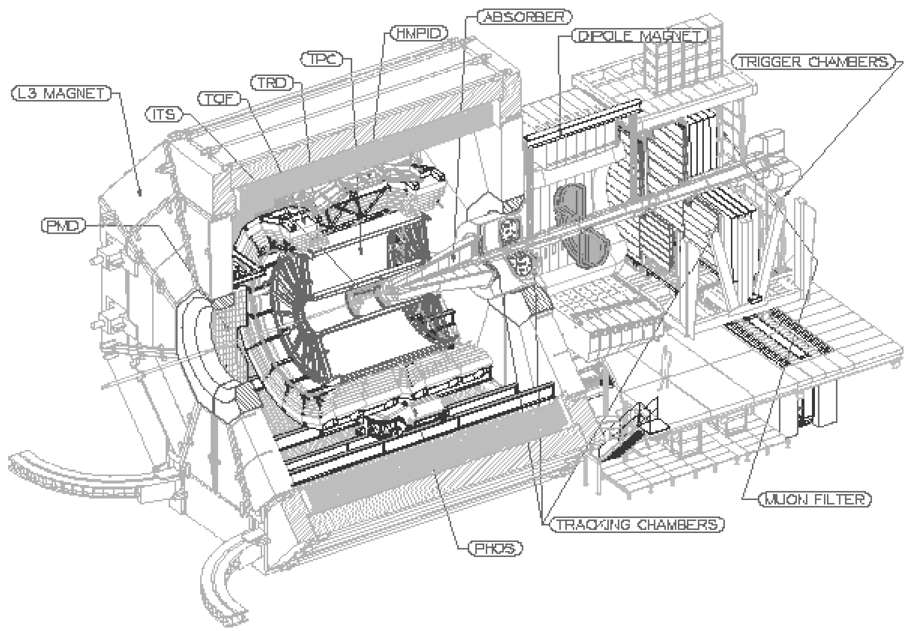


Fig. 4. Artists view of the ALICE detector.

ALICE (see figure 4) consists of a central part, which measures event-by-event hadrons, electrons and photons, and a forward spectrometer to measure muons. The central part, which covers polar angles from 45° to 135° over the full azimuth, is embedded in the large L3 solenoidal magnet. It consists of an Inner Tracking System (ITS) of high-resolution silicon tracking detectors, a cylindrical Time-Projection-Chamber (TPC), three particle identification arrays of Time-of-Flight (TOF), Ring Imaging Cherenkov (HMPID) and Transition Radiation (TRD) detectors and a single-arm electromagnetic calorimeter (PHOS). The forward muon arm (2°–9°) consists of a complex arrangement of absorbers, a large dipole magnet, and fourteen stations of tracking and triggering chambers. Several smaller detectors (ZDC, PMD, FMD, CASTOR, T0, V0) are located at forward angles.

In the following we will describe in more detail two of the ALICE subdetectors, which are essential for the measurement of quarkonia and open charm/bottom at midrapidity the time-projection-chamber [24] and the recently introduced Transition Radiations Detector (TRD) [25]. We will describe not only the layout of the detector but also the technical challenges and solutions to make them work in the high particle density environment of LHC Pb–Pb interactions. The inner tracking system [26], equally important for the capability of ALICE to measure high $p_{\mathrm{T}}$ electrons and open charm/bottom, will not be covered in this paper.

## *6.1. TPC*

### 6.1.1. TPC layout

The overall acceptance of the TPC is $-0.9 < \eta < 0.9$. To cover this acceptance the TPC is of cylindrical design with an inner radius of about 80 cm, an outer radius of about 250 cm, and an overall length in the beam direction of 500 cm. A schematic layout of the ALICE TPC is shown in figure 5.

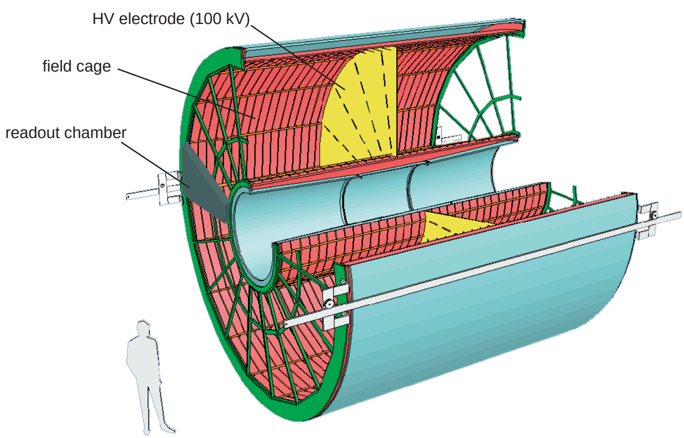


Fig. 5. ALICE TPC showing the central electrode, the field cage and the end plates.

The TPC field cage provides a highly uniform electrostatic field in a cylindrical high-purity gas volume to transport primary charges over long distances (2.5 m) towards the readout end-plates. The field configurations is defined by a high-voltage (up to 100 kV) electrode located at the axial center of the cylinder. A mixture of $NeCO_2$ is chosen as a drift gas, as is currently used in the NA49 (90%/10%) and CERES (80%/20%) SPS experiments.

The readout chambers (ROC) are basically conventional multiwire proportional chambers with cathode pad readout as used in many TPCs before. In detail, their construction, however, requires to overcome significant technical challenges as discussed below. The overall area to be instrumented is 32.5 m$^2$. The azimuthal segmentation of the readout plane follows that of the subsequent ALICE detectors, leading to 18 trapezoidal sectors, each covering 20 degrees in azimuth. The radial decrease of the track density leads to changing the requirements for the readout chamber design as a function of radius. Consequently, there will be two different types of readout chambers, the inner and outer chambers. Each outer chamber is further subdivided into two sections with different pad sizes, leading to a triple radial segmentation of the readout plane, with 557568 readout pads in total.

#### 6.1.2. TPC challenges

The most obvious negative consequence of a high track density is the corresponding high occupancy of the readout channels. In the following we show that a simple increase in the readout granularity would be of limited help if not accompanied by a number of other measures.

##### *6.1.2.1 Pad size*

A sufficient number of pads per charge cluster in terms of position resolution is 2–3. Thus an increase in the number of pads is sensible only if the induced charge from the (point-like) avalanche spreads over no more than 2–3 pads. This can be achieved by reducing the distance between anode wire and pad plane. However, at a certain point the distance HV-GND gets critical. There are also other reasons why it makes little sense to decrease the pad size beyond a certain limit: the width of the charge cloud after 250 cm of drift is of the order of mm depending on the choice of the drift gas and voltage. *I.e.*, any reduction of the pad beyond a certain size results in an oversampling of the track without any gain of information.

##### *6.1.2.2 Time direction*

The situation in time direction is similar: one could think of increasing the frequency of the time sampling, however, as diffusion occurs also in longitudinal direction this would result as well in an oversampling of the pulse. The choice of a shorter shaping time is limited by the fact that below 150–200 ns shaping time, the signal/noise ratio becomes critical.

##### *6.1.2.3 Optimization*

From the above considerations one is left with the following measures to optimize for best performance in a high density environment:

(1) Minimization of the diffusion, *i.e.* choice of a "cold" gas ($NeCO_2$, 90–10) and a high drift field (400 V/cm).

(2) Choice of a minimal pad area ($A = 30$ mm$^2$) which still gives a reasonable signal; this implies

   (a) the proper choice of the anode-pad distance (2 mm) to have the desired pad response function (PRF), and

   (b) a high gain, because the faint signal from the small pad needs high amplification. This can be done both by gas and electronic amplification, however, to optimize the signal/noise ratio ($S/N > 20$) a high gas gain ($2 \times 10^4$) and low electronic gain (12 mV/fC) is preferable. This choice should lead to a number of equivalent noise electrons below 1000.

(3) For a given pad area the proper choice of the aspect ratio ($4 \times 7.5$ mm$^2$) will further decrease the number of pads occupied by a cluster. The principal reason for this is that the tracks are oriented in a preferred direction, *i.e.*, radially.

*6.1.2.4 Long term stability*

In principle, the long term behavior of gaseous detectors is not testable, as the only halfway realistic test would require an exposure of the chambers at rates and durations comparable to the experimental conditions. For an expected running time of several years this is not possible for obvious reasons. One resorts, therefore, to short time tests with high intensity exposure to accumulate at least as much charge per unit length anode wire (where the amplification takes place) as in the experiment. In our case we exposed an anode area of about 1 cm$^2$ with a strong $^{55}$Fe source for about 2000 hrs. The resulting anode current of 25 nA was monitored and found to be stable for the whole measurement period. The corresponding charge/unit length of the anode wire is calculated to be 60 mC. This has to be compared with an estimated accumulated charge of 1.1 mC per cm wire and ALICE year (1 ALICE year = $10^6$ s).

*6.1.2.5 Space charge*

There are two distinct sources of space charge in the TPC drift volume:

(1) positive ions from primary ionization by a charged particle, and

(2) positive ion leaking back from the amplification zone into the drift space.

Owing to the much smaller mobility of the ions, as compared to the electrons, a quasi-stationary positive charge will distort the drift field significantly. While (1) is unavoidable and leads to distortions of the tracks of up to 0.5 mm for $NeCO_2$ as drift gas, (2) could cause much larger distortions if the ion feedback is not sufficiently blocked by the gate. This is particularly dangerous at the high amplification of $2 \times 10^4$ in the present ROC's. First tests on prototype chambers showed indeed that ions leak back into the drift space even with gate closed. Two-dimensional calculations of the field configuration revealed that the ion-leaks were located at the radial borders of the chamber, *i.e.*, at the discontinuities of the otherwise regular gating grid structure.

To circumvent the problem electrostatic "shims" were introduced to optimize the field geometry. The gating inefficiency was assessed by measuring the drift electrode current as a function of the gating offset voltage (*cf.* Fig. 6). At high gating offset voltage the measurement was limited by the sensitivity of the ammeter of $\approx 10$ pA. An upper limit of $0.5 \times 10^{-4}$ for the gating inefficiency was deduced. This, together with an amplification of $2 \times 10^4$ results in less than 20 ions/cm track coming from the amplification and is of the same order of magnitude as the ions from primary ionization.

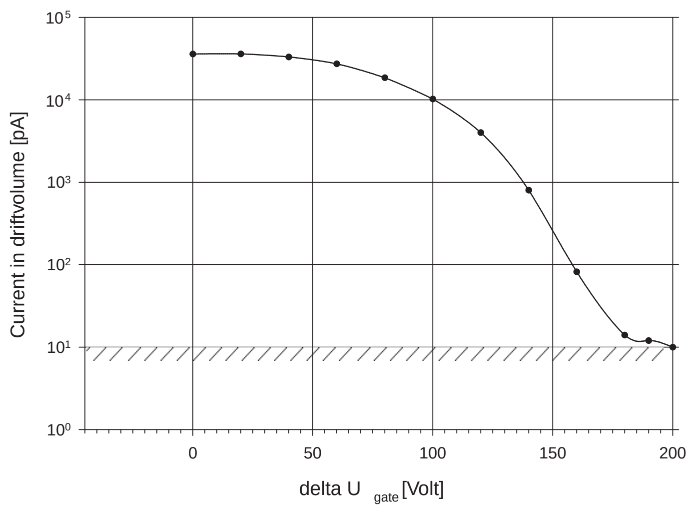


Fig. 6. Gating efficiency as a function of the offset voltage applied to the gating grid.

*6.1.2.6 High rate*

So far, previous TPC's have not yet been operated both at high gain and at high track density. It is thus questionable whether under those conditions the chamber can be operated stably at all. A test was performed at GSI employing a full size inner readout chamber. The chamber was irradiated with secondaries from a $^{12}$C beam hitting a thick target. By varying the target thickness and/or the beam intensity track densities from overlapping events, similar to LHC Pb + Pb collisions, could be reached. It turned out that the chamber could sustain several tens of $\mu$A anode current without signs of instability.

#### *6.1.2.7 Simulation results*

Even after the optimization steps described above one is left with an occupancy exceeding 50% at the innermost radius for an assumed multiplicity of $dN_{\mathrm{ch}}/dy = 8300$ plus background ($\approx 30\%$). Previous experience from the NA49 experiment demonstrated that the tracking efficiency is reduced dramatically for occupancies above 20%. The situation, however, is different for a fixed target experiment as NA49 and an experiment in collider geometry where the track density decreases quadratically with the radius. The ALICE tracking group has adopted novel tracking algorithms which are based on local methods, *i.e.*, the tracking starts at the outer parts of the TPC and proceeds to smaller radii. No global track model is needed in this case. Employing the Kalman filtering leads to an acceptable efficiency, *i.e.*, of 88% of all recognizable tracks are found with only 2% of fake tracks. At present, the momentum resolution is evaluated for the TPC only, *i.e.*, the connection to the other tracking detectors — ITS at small radii and TRD at large radii — is not included in the tracking algorithms. The momentum resolution $\Delta p/p$ at 1 GeV/$c$ is found to be 2.4%, which is close to the expectation of the Technical Design Report [24]. For high momentum tracks with $p > 5$ GeV/$c$ the resolution is at present $> 14\%$, clearly not good enough for high $p_{\mathrm{T}}$ physics. However, with the additional information from the other tracking detectors it is expected that the resolution for high momentum track is well below 5% [25].

The simulations yield a $dE/dx$ resolution of 8–9% in the high track density environment, while the resolution of a single, isolated track is $\approx 5\%$, which is close to the optimum. Thus the particle identification properties of the TPC are as good as they can possibly be under the given circumstances.

### *6.2. TRD*

Transition Radiation Detectors are used in high energy experiments to improve the identification of electrons with respect to pions for momenta between $\sim 1$ and 100 GeV/$c$ (see [27] for a review on TRD's). A proposal to add a TRD [28] to the ALICE experiment was approved in May 1999. Increasing the pion rejection power by at least a factor of 100 for momenta above 2 GeV/$c$, the TRD will allow the study, in the central region of the ALICE detector, of various aspects of di-electron physics. Among them are the production of quarkonia like $J/\Psi$ and $\Psi$' and the members of the $\Upsilon$-family, as well as the production of open charm and open beauty. An important aspect towards this goal is using the TRD as an on-line trigger for high momentum electrons [13, 28].

The ALICE TRD is composed of a radiator of up to 5 cm thickness and a photon detector, the latter being a drift chamber with a 3 cm drift zone and an amplification region of 5–6 mm. To cope with the large charged particles multiplicities expected in Pb + Pb collisions at LHC and to provide the necessary position resolution for track reconstruction, the readout of the drift chamber is done on a chevron pad plane. The chevron has a width of 10 mm and the chevron step is tailored to the anode wire pitch of 5 mm. Each pad is connected to a preamplifier whose output is fed into a Flash-ADC, sampling the drift time of up to 2 $\mu$s with a frequency of 10–20 MHz, . The detection gas of the drift chamber will be a Xe-based mixture to facilitate an efficient absorption of the transition radiation photons with typical energies between 4 and 30 keV. Six layers will surround the interaction point in full azimuth at radial distances from 2.9 to 3.7 meters and will match in polar angle the acceptance of the TPC ($45° < \Theta < 135°$). A total number of 540 sub-detectors will add up to a total surface of the TRD of about 800 m$^2$, with a typical single module dimensions of $1.1 \times 1.3$ m$^2$. With a pad size of about 6 cm$^2$, the total number of channels will be up to $1.2 \times 10^6$, depending on the final geometrical configuration.

#### 6.2.1. Pion rejection in high density environment

TRD's have proven to have pion rejection up to a factor of 500–1000 [27, 29, 30]. This number, however, will inevitably deteriorate in a high track density environment due to track misidentification. The decrease in efficiency is estimated by embedding tracks of fixed momentum into high multiplicity events ($dN_{\rm ch}/dy$ up to 8000). The result of the simulation is shown in figure 7 demonstrating that the performance is — even at the highest $dN/dy$ — close to the desired value of pion rejection factors $> 100$.

#### 6.2.2. High $p_{\rm T}$ electron trigger

One of the most essential aspects of the TRD is its capability to trigger on high $p_{\rm T}$ electrons. Only this feature allows at all the $\Upsilon$-measurement at mid rapidity, $J/\Psi$ spectroscopy at large momenta and jet detection with energies $> 100$ GeV. The most demanding part is the online tracking of the full event with high enough quality to select events that occur with probabilities of the order of $10^{-5}$.

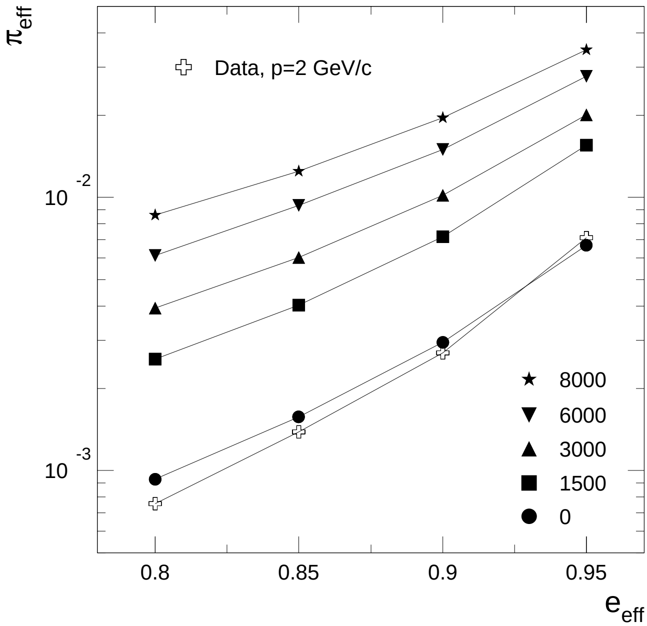


Fig. 7. The pion efficiency as a function of the electron efficiency for different event multiplicities and tracks of $p = 2$ GeV/$c$ total momentum.

The basic idea of the trigger system is to find high-momentum electrons and separate them from pions by a reconstructed track line and a transition radiation signature. The electron-pion separation is performed via the TR photons, which are primarily detected at the end of the drift-time. The track reconstruction algorithm takes into account the known track model for high-$p_{\rm T}$ particles. Such particle tracks are essentially perpendicular to the readout chambers pad plane, neglecting the Lorentz angle and the fact that the chambers are flat. Only a small number of channels is required to read out a complete track, allowing for the implementation of a track-let reconstruction engine in a highly parallel fashion ($\approx 70000$ units). The concept of the trigger is schematically shown in figure 8. Local track-lets are searched independently in all chambers of the detector in parallel processors; candidates of stiff track-let ($>$2 GeV/$c$) are shipped to a Global Tracking Unit (GTU) which selects high $p_{\rm T}$ tracks ($>$2.7 GeV/$c$) from the information sent to Local Tracking Units (LTU's). The result of the online tracking is transmitted to the ALICE trigger on a time scale below 6 $\mu$s. This time is still small compared to the drift time (88 $\mu$s) in the TPC, hence no information is lost.

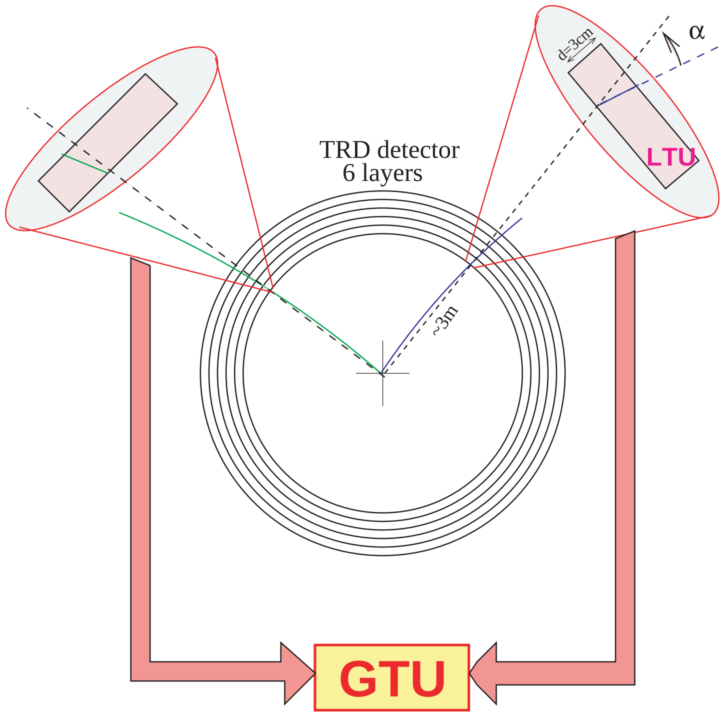


Fig. 8. Trigger scheme.

#### 6.2.3. *B* and *D* mesons

$B$ and $D$ mesons are identified via their semi-leptonic decay. The finite lifetime of $B$ and $D$ mesons, $c\tau = 496\ \mu$m and $c\tau = 315\ \mu$m , respectively, is used to separate electrons coming from $B$ and $D$ decays from those originating from other (promptly decaying) particles ($\pi^0, \rho, \omega, \phi, J/\Psi$) as described in the TRD TP [28]. It is based on the selection of non-primary high $p_{\mathrm{T}}$ electrons by optimizing selection criteria based on their transverse distance of closest approach to the primary vertex, $d_0$, and on their $p_{\mathrm{T}}$. The corresponding spectra are shown in figure 9 and figure 10.

Furthermore, since the quark and the gluon structure functions are likely to be different at LHC energies, one cannot use the Drell–Yan continuum as a convenient normalization for the $J/\Psi$ measurements. Moreover, the Drell–Yan cross section is expected to be completely masked by the open charm continuum. However, a direct measurement of the open charm yield simultaneously with the yield of quarkonia will provide a natural normalization and a gauge against which to quantify the expected suppression of quarkonia.

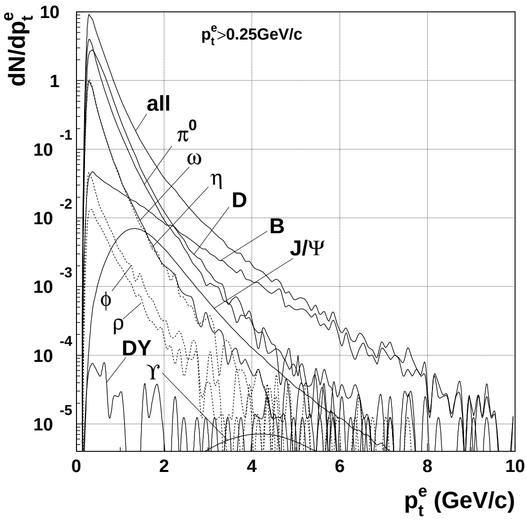


Fig. 9. Transverse momentum spectrum of single electrons into the TPC acceptance for the reaction Pb + Pb at $\sqrt{s} = 5.5$ TeV

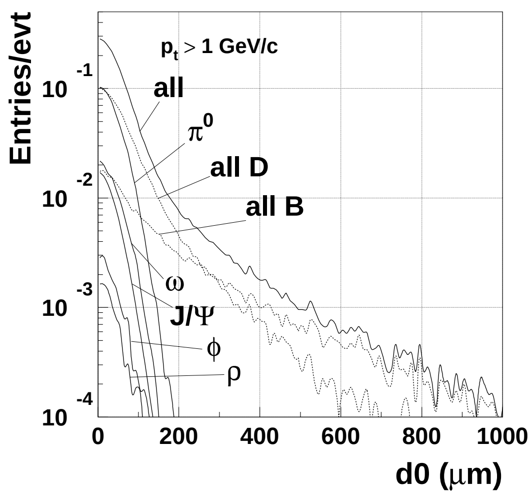


Fig. 10. Distribution of minimum transverse distance to primary vertex for electrons with transverse momenta of more than 1 GeV/$c$ originating from different parent particles. The effect of track resolution is included.

**6.2.4. Quarkonia**

The measurement of $J/\Psi$ at LHC energies is not statistics limited. However, several effects could obscure a clean interpretation of the measured $J/\Psi$ yield.

The decay of $B$ mesons can produce significant numbers of $J/\Psi$ mesons, especially at large $p_{\mathrm{T}}$. This is demonstrated in figure 11, where the transverse momentum distribution for directly produced $J/\Psi$ mesons is compared to the expected distribution of $J/\Psi$'s from $B$ decay. The calculations were performed assuming no suppression for the primary $J/\Psi$ mesons. If one wants to be sensitive to suppression factors of 10 or more and if one wants to address the $p_{\mathrm{T}}$ dependence of the suppression, it is obvious that the $B$ decay channel needs to be measured. Another issue is the secondary production of $J/\Psi$ mesons from the annihilation of $D$ mesons, *i.e.* the process $D+\overline{D} \rightarrow J/\Psi+\pi$. Estimates for the yield due to this process have recently been given [31]. For presently discussed values of the cross section for $D+\overline{D} \rightarrow J/\Psi+\pi$, the secondary production could seriously obscure the expected suppression in the plasma. It is, therefore, clear that a clean interpretation of $J/\Psi$ production data can only be obtained through a comprehensive measurement of open charm production.

Differently from the $J/\Psi$ the $\Upsilon$ is a rare particle: a $dN/dy(\Upsilon \rightarrow e^+e^-) = 10^{-5}$ (min bias) yields in total 25000 $\Upsilon$'s in the ALICE geometrical acceptance within $10^6$ s and at $L = 10^{27}$ cm$^{-2}$s$^{-1}$. Without $\Upsilon$-trigger, about 200 would be recorded onto tape. A simulation of the TRD trigger capabilities of correlating high $p_{\mathrm{T}}$ tracks within $< 6$ $\mu$s yields an enrichment factor of about 15 for $\Upsilon$'s. Thus, only with the trigger capabilities of the TRD a $\Upsilon$ measurement at mid-rapidity seems possible.

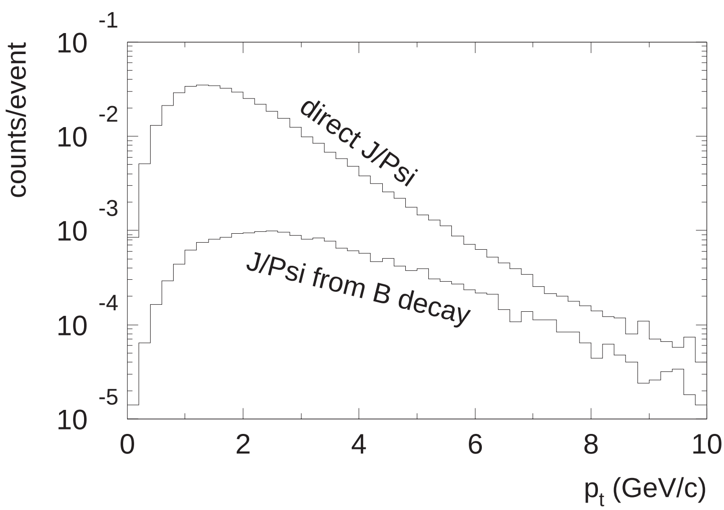


Fig. 11. Transverse momentum distribution of directly produced $J/\Psi$ mesons compared to the expected distribution of $J/\Psi$'s from $B$ decay.

## 7. Summary and conclusions

In this paper we have put emphasis on two important aspects of the CERN-LHC experiment ALICE: (a) the unpreceded high beam energy at the LHC opens a regime of high density partonic interactions which goes substantially beyond SPS and RHIC. All relevant system parameters — energy density, QGP lifetime, freeze-out volumina — will be up to one order of magnitude higher than ever before; (b) the recent addition of a TRD to the ALICE experiment opens new physics perspectives: the $J/\Psi$ and the $\Upsilon$-family becomes accessible at mid-rapidity, and, moreover, the yields of open and hidden charm and bottom production can be related to each other.

## REFERENCES


[1] F. Abe *et al.*, *Phys. Rev.* **D41**, 2330 (1990).

[2] C. Albajar *et al.*, *Nucl. Phys.* **B335**, 261 (1990).

[3] S.A. Bass *et al.*, *Nucl. Phys.* **A661**, 205c (1999).

[4] K.J. Eskola, *Nucl. Phys.* **A698**, 78c (2002).

[5] I. Abt *et al.*, *Nucl. Phys.* **B407**, 515 (1993); M. Derrick *et al.*, *Phys. Lett.* **B316**, 145 (1993); C. Adloff *et al.*, *Nucl. Phys.* **B497**, 515 (1997).

[6] K.J. Eskola, *Nucl. Phys.* **A590**, 383c (1995).

[7] J. Schukraft, *Nucl. Phys.* **A698**, 287c (2002).

[8] X.-N. Wang, M. Gyulassy, *Phys. Rev. Lett.* **86**, 3496 (2001); J. Jalilian-Marian, Xin-Nian Wang, *Phys. Rev.* **D63**, 096001 (2001); Shi-Yuan Li, Xin-Nian Wang, *Phys. Lett.* **B527**, 85 (2002).

[9] M. Arnedo, *Phys. Rep.* **240**, 301 (1994).

[10] R. Baier *et al.*, *Nucl. Phys.* **B483**, 291 (1997); M. Gyulassy *et al.*, *Phys. Rev. Lett.* **85**, 5535 (2000); U.A. Wiedemann, *Nucl. Phys.* **B588**, 303 (2000).

[11] L.V. Gribov *et al.*, *Phys. Rep.* **100**, 1 (1983); A.H. Müller, J. Qui, *Nucl. Phys.* **B268**, 427 (1986); J.-P. Blaizot, A.H. Müller, *Nucl. Phys.* **B289**, 847 (1987); K.J. Eskola, *Prog. Theor. Phys. Suppl.* **129**, 1 (1997).

[12] D. Kharzeev, E. Levin, *Phys. Lett.* **B523**, 79 (2001).

[13] P. Braun-Munzinger, *Nucl. Phys.* **A661**, 261c (1999).

[14] H. Satz, *Nucl. Phys. Proc. Suppl.* **94**, 204 (2001).

[15] K.J. Eskola, K. Kajantie, P.V. Ruuskanen, K. Tuominen, *Nucl. Phys.* **B570**, 379 (2000).

[16] R. Stock, Event–by–Event Analysis of Ultrarelativistic Heavy Ion Collisions, in: Proceedings of the NATO Advanced Study Workshop on Hot Hadronic Matter: Theory and Experiment, Divonne-les-Bains, France, 27 June–1 July 1994; H. Appelshäuser *et al.*, *Phys. Lett.* **B450**, 679 (1999); J.G. Reid, *Nucl. Phys.* **A661**, 407c (1999).

[17] P. Braun-Munzinger, I. Heppe, J. Stachel, *Phys. Lett.* **B465**, 15 (1999).

[18] S. Digal, P. Petreczky, H. Satz, *Phys. Lett.* **B514**, 57 (2001); *Phys. Rev.* **D64**, 094015 (2001).

[19] P. Braun-Munzinger, J. Stachel, *Phys. Lett.* **B490**, 196 (2000).

[20] R. Gavai, D. Kharzeev, H. Satz, G.A. Schuler, K. Sridhar, R. Vogt, *Int. J. Mod. Phys.* **A10**, 3043 (1995).

[21] A. Drees, *Nucl. Phys.* **A698**, 331c (2002).

[22] D. Srivastava, *Eur. Phys. J.* **C10**, 487 (1999).

[23] D. Brandt, CERN-LHC-Project-Report-450.

[24] Technical Design Report, CERN/LHCC 2000-001.

[25] Technical Design Report, CERN/LHCC 2001-021.

[26] Technical Design Report, CERN/LHCC 1999-012.

[27] B. Dolgosheim, *Nucl. Instrum. Methods Phys. Res.* **A326**, 434 (1993).

[28] Addendum to the ALICE Technical Proposal, CERN/LHCC 99-13.

[29] G. Bassompierre *et al., Nucl. Instrum. Methods Phys. Res.* **A411**, 63 (1998).

[30] K. Ackerstaff *et al., Nucl. Instrum. Methods Phys. Res.* **A417**, 230 (1998).

[31] C.M. Ko, X.N. Wang, X.F. Zhang, *Phys. Lett.* **B444**, 237 (1998).